

## Boosting the mechanical properties at 815°C of laser-directed energy-deposited Inconel 625 alloy by introducing the Laves phase

Zuo Li , Xin Lin , Xin Hou , Zhiwei Hao , Wei Fan , Chongliang Zhong , Hua Tan , Yiyi Zhou & Yi Min Xie

To cite this article: Zuo Li , Xin Lin , Xin Hou , Zhiwei Hao , Wei Fan , Chongliang Zhong , Hua Tan , Yiyi Zhou & Yi Min Xie (2026) Boosting the mechanical properties at 815°C of laser-directed energy-deposited Inconel 625 alloy by introducing the Laves phase, *Virtual and Physical Prototyping*, 21:1, e2613183, DOI: [10.1080/17452759.2026.2613183](https://doi.org/10.1080/17452759.2026.2613183)

To link to this article: <https://doi.org/10.1080/17452759.2026.2613183>



© 2026 The Author(s). Published by Informa UK Limited, trading as Taylor & Francis Group



Published online: 16 Jan 2026.



Submit your article to this journal [↗](#)



Article views: 147



View related articles [↗](#)



View Crossmark data [↗](#)

# Boosting the mechanical properties at 815°C of laser-directed energy-deposited Inconel 625 alloy by introducing the Laves phase

Zuo Li<sup>a,b,c</sup>, Xin Lin<sup>b,c</sup>, Xin Hou<sup>d</sup>, Zhiwei Hao<sup>b,c</sup>, Wei Fan<sup>b,c</sup>, Chongliang Zhong<sup>e</sup>, Hua Tan<sup>b,c</sup>, Yiyi Zhou<sup>a</sup> and Yi Min Xie<sup>a,f</sup>

<sup>a</sup>College of Future Technologies, Hohai University, Changzhou, People's Republic of China; <sup>b</sup>State Key Laboratory of Solidification Processing, Northwestern Polytechnical University, Xi'an, People's Republic of China; <sup>c</sup>Key Laboratory of Metal High Performance Additive Manufacturing and Innovative Design, MIIT China, Northwestern Polytechnical University, Xi'an, People's Republic of China; <sup>d</sup>Beijing Institute of Remote Sensing Equipment, Beijing, People's Republic of China; <sup>e</sup>Fraunhofer Institute for Manufacturing Technology and Advanced Materials IFAM, Dresden, Germany; <sup>f</sup>Centre for Innovative Structures and Materials, School of Engineering, RMIT University, Melbourne, Australia

## ABSTRACT

This study aims to enhance the high-temperature mechanical properties of the laser-directed energy-deposited Inconel 625 alloy. Varied sizes, morphologies and volume fractions of the Laves phase were effectively regulated, high-temperature tensile properties and stress rupture life were systematically investigated, and the underlying mechanisms were revealed thoroughly. The results demonstrate that when the Laves phase morphology transitions from long-stripped to granular, with optimised dimensions (length: 1–2  $\mu\text{m}$ , width: 0.2–0.6  $\mu\text{m}$ ) and a precise volume fraction of 1.2%, the alloy exhibits a notable enhancement in mechanical performance: yield strength increases from 192.67 MPa to 217.33 MPa, tensile strength rises from 324.67 MPa to 348.33 MPa and stress rupture life extends from 24 h to 31 h. The boost in the high-temperature tensile strength was attributed to the precipitation of  $\gamma'$  and  $\delta$  phases near the Laves phase or the pinning effect at the Laves/ $\gamma$  interface. The extended stress rupture life results from  $\delta$  phases hindering dislocation motion while promoting dynamic recovery. This study confirmed that retaining a controlled amount of Laves phase significantly enhances the mechanical properties of the Inconel 625 alloy, providing valuable insights for laser additive manufacturing and repaired nickel-based superalloy above 800°C.

## ARTICLE HISTORY

Received 5 November 2025  
Accepted 29 December 2025

## KEYWORDS





Laser directed energy deposition; Inconel 625; laves phase; stress rupture life; dynamic recovery

## 1. Introduction

Nickel-based superalloy Inconel 625 (GH625) is widely used in high-temperature components in fields such as aerospace, energy and chemical industries due to its excellent strength, outstanding resistance to oxidation, corrosion, and fatigue [1,2]. Examples include gas turbine blades, heat exchanger pipes, and hot-end components of aircraft engines [3,4]. However, these key components often suffer damage or even failure due to fatigue, creep, wear or corrosion in extremely demanding service environments [5,6]. The overall replacement cost is high and the process takes a long time. Therefore, developing efficient and reliable remanufacturing and repair technologies holds significant economic and strategic value [7]. Laser directed energy deposition (DED-LB) has emerged as one of the most

promising technologies for the repair and remanufacturing of high-performance metal components due to its advantages such as high energy density, high degree of formability and controllable heat input [8,9]. This technology lies in the process of layer-by-layer deposition, which precisely reconstructs a three-dimensional solid with properties comparable to or even superior to those of the base material in the damaged zone, restoring the geometric shape and service function of the part.

The microstructure of Inconel 625 alloy deposited by DED-LB is completely different from that of traditional forging or casting [10–12]. The unique non-equilibrium metallurgical characteristics of laser rapid melting and solidification (with cooling rates up to  $10^3 \sim 10^6$  K/s) significantly alter the microstructure evolution path and the final phase composition of alloys. Inconel 625 alloy is a

**CONTACT** Xin Lin  xlin@nwpu.edu.cn  State Key Laboratory of Solidification Processing, Northwestern Polytechnical University, Xi'an, Shaanxi 710072, People's Republic of China; Key Laboratory of Metal High Performance Additive Manufacturing and Innovative Design, MIIT China, Northwestern Polytechnical University, Xi'an, Shaanxi 710072, People's Republic of China; Yiyi Zhou  yiyi.zhou@hhu.edu.cn  College of Future Technologies, Hohai University, Changzhou, Jiangsu 213200, People's Republic of China

© 2026 The Author(s). Published by Informa UK Limited, trading as Taylor & Francis Group

This is an Open Access article distributed under the terms of the Creative Commons Attribution-NonCommercial License (<http://creativecommons.org/licenses/by-nc/4.0/>), which permits unrestricted non-commercial use, distribution, and reproduction in any medium, provided the original work is properly cited. The terms on which this article has been published allow the posting of the Accepted Manuscript in a repository by the author(s) or with their consent.

solid solution strengthened alloy with  $\gamma$ -Ni as the austenitic matrix, and its main strengthening elements such as niobium (Nb) and molybdenum (Mo) have high solubility in the  $\gamma$  phase [13]. Under equilibrium solidification conditions, these elements are fully dissolved in the matrix, exerting a strong solid solution strengthening effect. However, during the rapid solidification process in laser additive manufacturing, solute elements (especially Nb) undergo severe segregation at the solidification interface, resulting in the accumulation of a large amount of Nb, Mo, and other elements in the interdendritic regions of the final solidification [14], which is highly prone to the formation of brittle intermetallic compound phases – Laves phases (typically Ni, Nb, Mo, with a chemical formula approximately  $(\text{Ni, Fe, Cr})_2(\text{Nb, Mo, Ti})$ ) [15–17].

For a long time, the Laves phase has been generally regarded as a detrimental phase in the microstructure of additively manufactured Inconel 625 [18–20]. Its massive, continuous network or lamellar morphology severely disrupts the continuity of the matrix, serving as a source for the initiation of microcracks and significantly degrading the plasticity and toughness [21–23]. However, recent studies have shown that by precisely adjusting the laser process parameters (such as laser power, scanning speed, powder feeding rate, etc.), the morphology, size, and distribution of Laves phases can be changed, transforming them from a continuous brittle network structure to discrete granular or block-like forms [24,25]. This morphological Laves phase may no longer merely be a source of crack initiation, but instead plays the role of a strengthening phase [26,27]. At present, the reports on the Laves phase as a strengthening phase mainly focus on high-entropy alloys or precipitation-strengthened superalloys [24,26]. Among them, the most typical one is Inconel 718 alloy [25]. For instance, in our previous work, when a certain amount of Laves phase with controlled dimensions (average length  $\sim 0.55 \mu\text{m}$ , average width  $\sim 0.42 \mu\text{m}$ , volume fraction  $\sim 1.55\%$ ) is retained within the alloy, the room-temperature strength and plasticity can be simultaneously enhanced [24]. When larger-sized Laves phases (length  $\sim 3.69 \mu\text{m}$ ; width  $\sim 1.94 \mu\text{m}$ ; aspect ratio  $\sim 1.99$  and volume fraction  $\sim 1.55\%$ ) are preserved in the alloy, the stress-rupture (SR) life of the alloy can exceed that of the forged piece by a factor of three [25]. The above research clearly demonstrates that the Laves phase plays a role in the strengthening phase within the materials.

Unlike Inconel 718 alloy, Inconel 625 alloy is a type of solid-solution strengthened high-temperature alloy. Therefore, conventional research and process development have generally focused on eliminating the Laves phase as thoroughly as possible through means such as increasing energy input and conducting high-

temperature heat treatments (such as solution treatment), promoting the redissolution of segregated elements, and obtaining a uniform single-phase  $\gamma$  structure to restore the strength and plasticity [28,29]. However, the validity of this traditional approach needs to be reexamined when it comes to high-temperature (typically above  $600^\circ\text{C}$ ) applications [30]. High-temperature strength, especially creep resistance, not only depends on the solid-solution strength of the matrix but also relies on stable and dispersed second-phase strengthening. Completely eliminating the Laves phase also means eliminating its potential as a strengthening phase. Currently, most of the research on the high-temperature SR or creep properties of Inconel 625 alloy by laser additive manufacturing focuses on the laser powder bed fusion (LPBF) technology [28,30–32], and rarely involves DED-LB [33]. Different from DED-LB technology, the Laves phase within Inconel 625 alloy fabricated by LPBF, its size generally ranging from several tens to several hundred nanometers [34,35]. Perhaps the adjustable range of its size is very limited for Inconel 625 alloy fabricated by LPBF, and the research on the influence of Laves phase regulation on the high-temperature mechanical properties of the alloy has also been overlooked. Furthermore, although the high-temperature mechanical properties of laser additive manufacturing Inconel 625 have been extensively investigated and discussed [2,21,30,36–38], only a few works focused on the aeroengine service temperature environment [28,39]. Most of the current reports on the high-temperature mechanical properties of Inconel 625 alloy are based on temperatures below  $800^\circ\text{C}$  (dissolution temperature of the  $\gamma''$  phase). However, Inconel 625 alloy commonly works at elevated temperatures of  $800$ – $900^\circ\text{C}$ , i.e. in casing and guide vane of aeroengines. When the temperature exceeds  $800^\circ\text{C}$ , the  $\gamma''$  phase will transform into the  $\delta$  phase [40]. At this point, how the  $\delta$  phase will affect the high-temperature mechanical properties of the alloy remains to be further investigated.

Herein, the laser direct energy deposition technology was selected to investigate the influence of Laves phase characteristic parameters (morphology, size and volume fraction) on the SR life at  $815^\circ\text{C}$  of Inconel 625 alloy. The high-temperature SR properties of alloys containing different-sized Laves phases were characterised. A comparative analysis of the microstructure evolution of Inconel 625 alloys with different-sized Laves phases before and after high-temperature loading was conducted in detail, and the intrinsic influence mechanism and strengthening mechanism of Laves phases on the high-temperature mechanical properties of the alloy were unveiled.

## 2. Experimental details

### 2.1. DED-LB process

The deposition of Inconel 625 block specimens in this work was carried out on the LSF-S6000A DED-LB system independently developed by the State Key Laboratory of Solidification Technology. The experimental equipment is shown in Figure 1(a). This system includes: a CP6000 type (with a maximum power of 6 kW) semiconductor continuous laser, a DSPF-2 type high-precision adjustable automatic powder feeder, a coaxial powder feeding nozzle, an inert atmosphere processing chamber, and a five-axis four-link numerical control worktable, etc. The carrier gas and protective gas used in the experiment were all high-purity argon. The spherical Inconel 625 alloy powder used in the DED-LB experiment was prepared by the Plasma Rotating Electrode Process (PREP) method. The particle size of the powder was 53~150  $\mu\text{m}$ . The main chemical composition of the powder is shown in Table 1. The microscopic morphology is as shown in Figure 1(b). The powder has a high sphericity and a relatively uniform particle size

distribution. Before the experiment, the alloy powder was subjected to vacuum drying treatment. The drying temperature was 120°C and the drying time was 2~3 h. After the heat preservation, it was cooled to room temperature in a vacuum furnace and then taken out. The substrate used in the experiment was forged Inconel 625 alloy. A substrate block with dimensions of 80 mm (length)  $\times$  40 mm (width)  $\times$  40 mm was obtained through wire cutting for deposition. The surface oxide scale was removed using sandpaper, and a metallic luster was achieved through grinding. Subsequently, the sample was cleaned with acetone and dried.

Table 2 presents the process parameters for bulk sample of Inconel 625 alloy. The deposition process is as follows: firstly, the forged Inconel 625 alloy substrate is fixed on the computer numerical control (CNC) worktable. Then, the protection chamber is filled with high-purity argon gas until the oxygen content in the chamber is lower than 100 ppm, and the deposition experiment begins. The scanning strategy employed in this experiment is the reciprocating weaving scanning, as shown in Figure 1(c). After the experiment, the as-

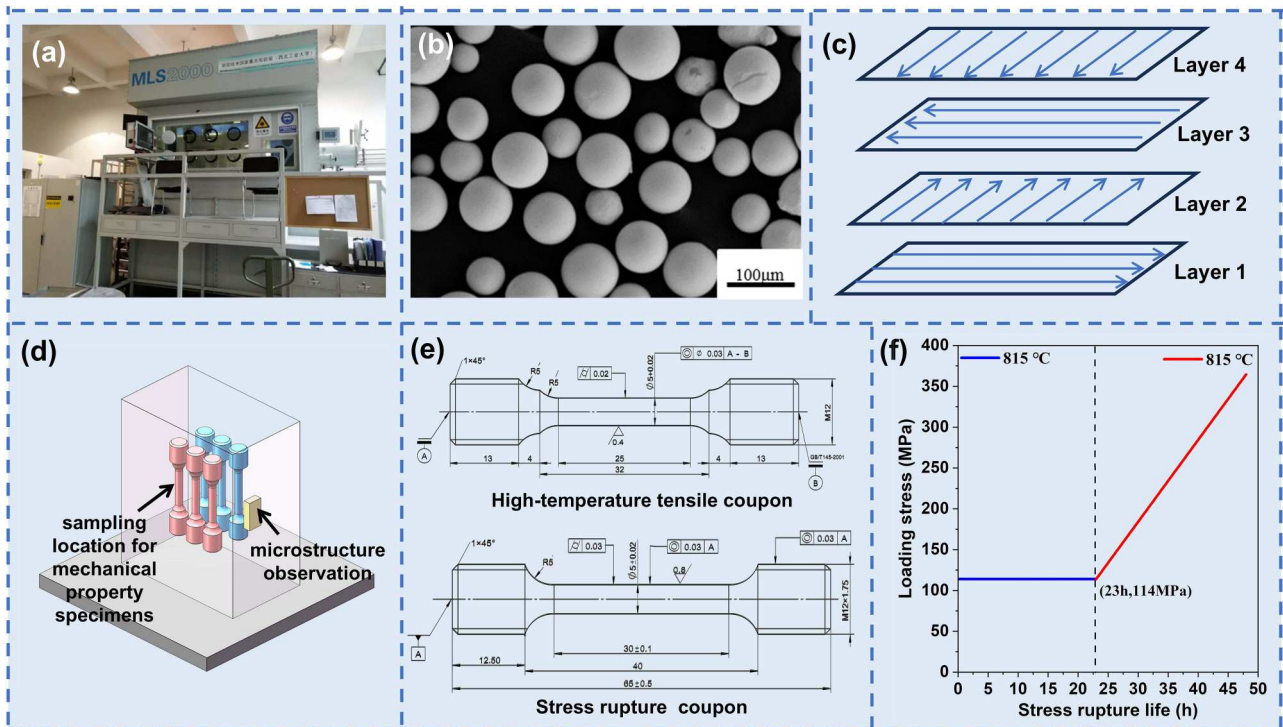


**Figure 1.** The details of sample preparation and mechanical properties tests. (a) DED-LB equipment; (b) Inconel 625 spherical powder; (c) reciprocating weaving scanning; (d) sampling location for mechanical property specimens; (e) high-temperature tensile coupon and stress rupture coupon; (f) profile of loading stress and stress rupture life.

**Table 1.** The nominal chemical composition of Inconel 625 alloy powder.

| Element        | Cr   | Nb   | Mo  | Fe   | Al   | Ti   | C     | Ni      |
|----------------|------|------|-----|------|------|------|-------|---------|
| Content (wt.%) | 21.9 | 3.53 | 8.7 | 3.93 | 0.25 | 0.20 | 0.042 | Balance |

**Table 2.** The processing parameters of Inconel 625 alloy fabricated by DED-LB process.

| Laser type    | Laser power (W) | Scanning speed (mm/s) | Powder feeding rate (g/min) | Laser diameter (mm) |
|---------------|-----------------|-----------------------|-----------------------------|---------------------|
| Semiconductor | 3500            | 20                    | 25                          | 3                   |

**Table 3.** The heat treatment regime of Inconel 625 alloy fabricated by DED-LB process.

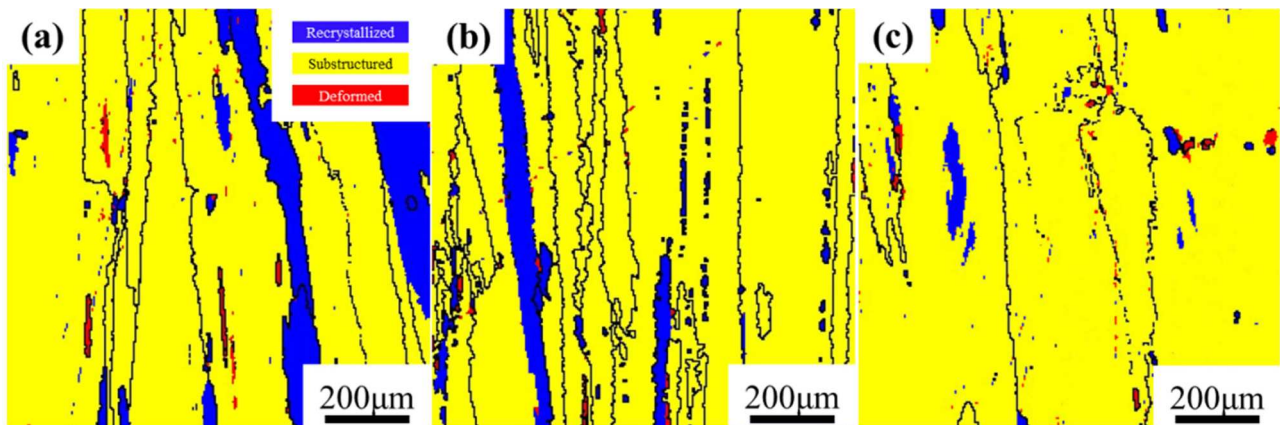
| Solution treatment | Name |
|--------------------|------|
| 1050°C, 15 min/WC  | S-15 |
| 1050°C, 45 min/WC  | S-45 |

built samples are cooled to room temperature in an inert atmosphere before being removed. In order to study the influence of Laves phase characteristic parameters on the mechanical properties, an appropriate solution heat treatment regime is necessary. The heat treatment details are shown in Table 3. Based on the previous work of regulating Laves phase within Inconel 718 alloy [24,25], 1050°C is a proper choice. Firstly, 1050°C is lower than the recrystallisation temperature (1100°C) of Inconel 625 alloy [41,42], thus preventing the alloy from undergoing recrystallisation due to the heat treatment process. The recrystallisation maps of the Inconel 625 alloy before and after heat treatment are shown in Figure 2. Figure 2(a) shows the as-built state, and Figure 2(b) and (c) represent the results after heat treatment for 15 min and 45 min, respectively. The blue region represents the recrystallised grains. It can be observed that when the solution time is extended from 0 min to 45 min, the alloy does not undergo recrystallisation. Therefore, the solution temperature of 1050°C is appropriate. Secondly, at a temperature of 1050°C, by extending the solution time, various characteristic parameters of Laves phases can be obtained

easily, thereby enabling the quantitative control of Laves phases [25,43].

## 2.2. Microstructure characterisation

The cross-section of the Inconel 625 sample was cut by electrical discharge wire cutting, and then it was embedded, ground, and mechanically polished to prepare the metallographic sample. After polishing, chemical corrosion was performed with the following reagent ratio: 25 g CrO<sub>3</sub> + 150 ml HCl + 50 ml H<sub>2</sub>O. The corrosion time was 20 s at room temperature. The macroscopic grain morphology of the metallographic sample was observed using the Keyence VHX-2000 super-depth optical microscope. The phase distribution in the metallographic sample was observed using the TESCAN VEGA II-LMH and the ZEISS SUPRA scanning electron microscope (SEM). The element distribution of the precipitation phase was analyzed using EDS energy spectrum analysis equipped on the SEM and Shimadzu EPMA-1720 electron probe. To study the microstructure evolution mechanism of Inconel 625 alloy during heat treatment and the dynamic softening effect during the high-temperature loading process, the microstructure of the relevant samples was further characterised by EBSD technology. The metallographic samples for EBSD analysis were rough-ground and fine-ground on 400#, 800# and 1500# sandpapers, then they were automatically polished using the automatic grinding and polishing machine. Finally, in order to remove the residual stress on the sample surface, the polished samples were vibrated and polished by a vibration polishing machine for 2 h. The EBSD test was conducted on a TESCAN VEGA II-LMH type SEM equipped with an EBSD probe, with a step size of 5 µm. Furthermore, the statistics regarding the volume fraction of Laves phases were conducted using the Image Pro

**Figure 2.** The maps of recrystallised grains within the Inconel 625 alloy before and after heat treatment. (a) as-built; (b) S-15 sample; (c) S-45 sample.

Plus (IPP) software in this work. In order to assure the accuracy of the statistical results, it is usually necessary to select about 20~25 original SEM images for the statistics. First, import the original SEM image into the IPP software, and then use the measurement function to calibrate the scale of the image. Based on this, the 'count/size' function was selected to convert the original SEM image into a binary image. Then, the area percentage was used as the statistical parameter. After conducting multiple statistics, the average value and standard deviation can be calculated.

The high-temperature mechanical properties tests in this work were conducted at the Northwest Institute for Non-ferrous Metal Research. Figure 1(d) shows the sampling method and location of the performance test samples. The dimensions of the specimens used in the high-temperature tensile tests are presented in Figure 1(e), and the experimental temperature was 815°C. The tensile direction was parallel to the laser deposition direction, and the tensile test refers to the national standard GB/T 228.2–2015. The loading rate before yielding was 0.6 mm/min, and it was 3 mm/min after the extensometer was removed. The sample size used in the SR test also is shown in Figure 1(e). The loading temperature is still 815°C, and the external load is 114 MPa. After 23 h, the load is increased by 10 MPa every hour until the specimen failed. The profile of loading stress and stress rupture life is shown in Figure 1(f). The basis standard for the SR test is GJB3317-98, which complies with the test specifications for aerospace superalloys. It is necessary to emphasise that, whether it is the high-temperature tensile test or the SR test, each test condition will have the experiment repeated three times, and then the average value and standard deviation will be calculated to assure the reliability of the test results. After conducting the high-temperature tensile and SR tests, the specimens were cut along the loading direction into thin slices with a thickness of 0.5 mm. These thin slices were then ground on sandpaper to a size of 50  $\mu\text{m}$  and subsequently prepared into transmission specimens with a diameter of 3 mm using the electrolytic double spray method. The electrolyte ratio was 10:90 (volume ratio) of perchloric acid ( $\text{HClO}_4$ ) to ethanol ( $\text{C}_2\text{H}_5\text{OH}$ ). The dislocation configurations within Inconel 625 alloy were observed using a Tecnai-G2 F30 transmission electron microscope (TEM) during the high-temperature deformation process.

### 3. Results and discussion

#### 3.1. Microstructure evolution after heat treatment regimes

Figure 3 shows the macro and microstructure characteristics of DED-LB fabricated Inconel 625 alloy with

different states and wrought samples. With the extension of the solution treatment time from 0 min to 45 min, the grain characteristics of the alloy do not change significantly, and all present columnar grains with epitaxial growth, as shown in Figure 3(a–c). The size of columnar grains is characterised by the equivalent circular diameter in this work. According to the statistics, the average size of columnar grain sizes within the as-built, S-15, and S-45 samples is 132.04  $\mu\text{m}$ , 71.1  $\mu\text{m}$ , and 109.92  $\mu\text{m}$ , respectively. This statistical result can be proven by the EBSD results shown in Figure 11 later. For comparison, the wrought sample of Inconel 625 is primarily composed of equiaxed grains in Figure 3(d) and the average diameter is approximately 50  $\mu\text{m}$ .

In addition to the grains, the long-striped Laves phases were observed between the dendrites from Figure 3(e). The morphology of Laves phases after different solution times at 1050°C was statistically analyzed and the results of their length, width, and aspect ratio are shown in Figure 4. In terms of as-built sample, the length of the Laves phase mainly ranges from 3 to 8  $\mu\text{m}$ , with a width of approximately 1  $\mu\text{m}$ , and most of them have a length-to-width ratio greater than 3 in Figure 4(a). The volume fraction of Laves phase is about 13.2% and the content of Nb element in the matrix is 1.92%, as shown in Table 4. When the solution time was extended to 15 min, the Laves phase gradually transformed from a long strip-like shape to a short rod-like or granular shape, as shown in Figure 3(f), and the volume fraction rapidly dropped to 1.2%. The length of Laves phase is mainly 1 to 2  $\mu\text{m}$ , and the width is from 0.2 to 0.6  $\mu\text{m}$  from Figure 4(b). When the solution time is 45 min, the Laves phase has become even more refined and has completely transformed into a granular form in Figure 3(g). At this time, since the size of Laves phase is similar to that of the carbides and both appear white under backscattered electron image (BSE), it is difficult to distinguish them. However, Figure 3(i) and (j) indeed has confirmed the existence of Laves phase and carbides, and this will be elaborated in the following paragraph. If the granular carbides are also counted as Laves phases for statistics, then the volume fraction of Laves phases would be at most 0.9%, and the aspect ratio is close to 1. On the other hand, the microstructure of the wrought Inconel 625 is characterised by a small amount of particle-like MC-type carbides with a size of approximately 1–5  $\mu\text{m}$ , which are distributed along grain boundaries and twinning boundaries, as well as large blocks of Nb-rich carbides and Ti-rich nitrides with a size of more than 5  $\mu\text{m}$ , as shown in Figure 3(h). The crystal

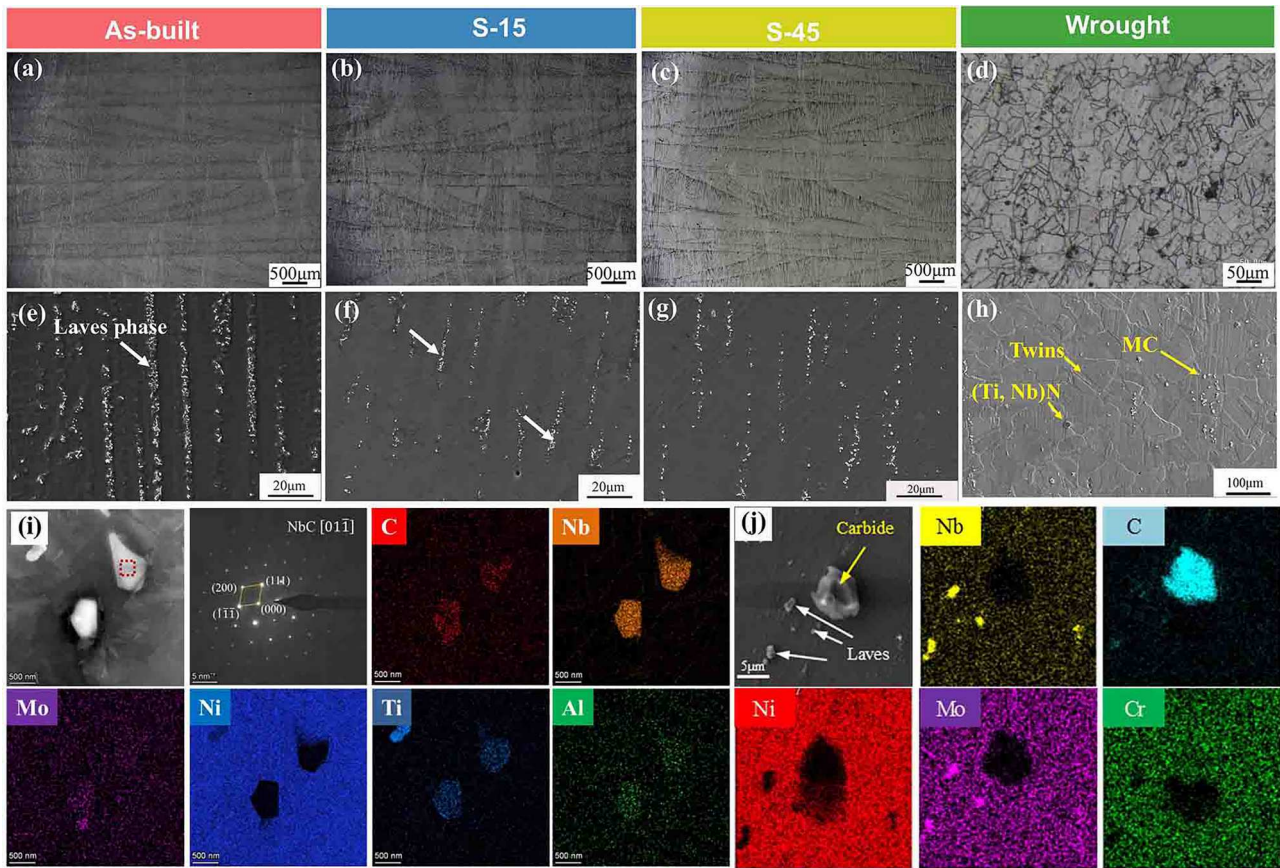


**Figure 3.** The microstructure characteristics of Inconel 625 alloy after different solution times and wrought Inconel 625. (a–d) grain features; (e–g) Laves phase evolution; (h) the precipitated phase of wrought Inconel 625; (i) EDS mapping results of NbC; (j) EDS mapping results of Laves phase.

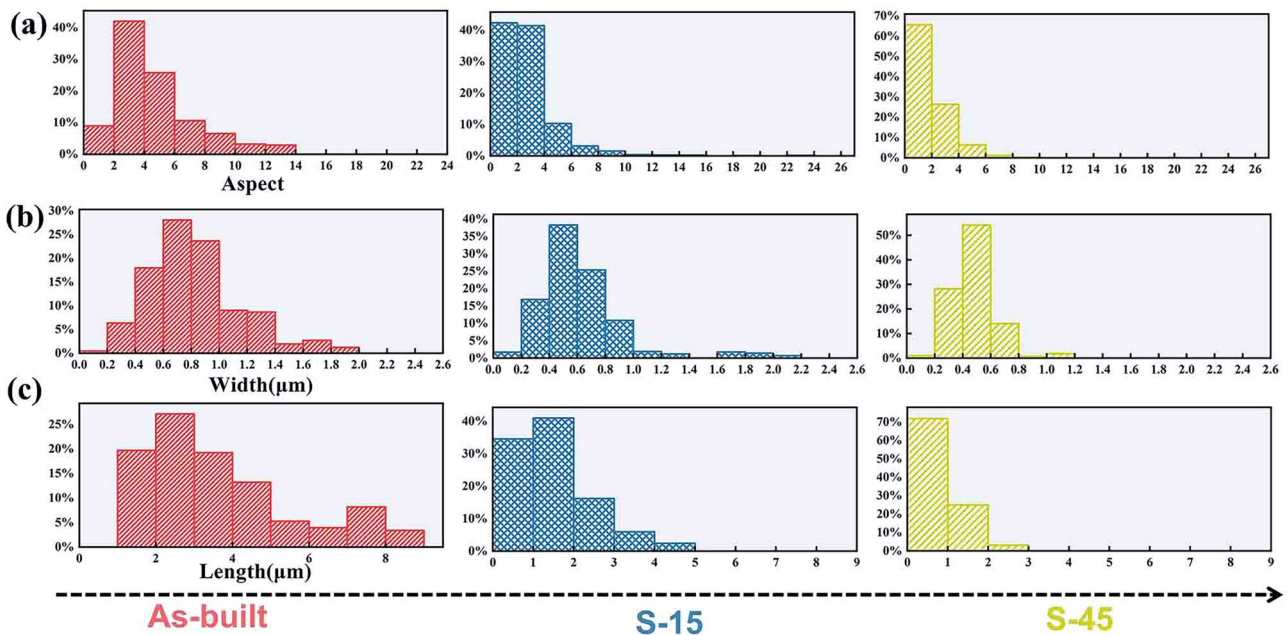


**Figure 4.** Statistical results of the evolution of Laves phase: (a) as-built; (b) S-15; (c) S-45.

**Table 4.** The statistical results of the Laves phase volume fraction and the Nb element content in the matrix of laser-directed energy-deposited Inconel 625 alloy.

| Sample   | The volume fraction of Laves phase | Mass fraction of Nb element in $\gamma$ matrix |
|----------|------------------------------------|--|
| As-built | 13.2 vol.%                         | 1.92 wt%                                       |
| S-15     | 1.2 vol.%                          | 2.92 wt%                                       |

structure of the MC-type carbides is of the face-centered cubic (FCC) structure as the matrix  $\gamma$ , and they have good bonding with the matrix.

Furthermore, the sizes of some specific particle phases are smaller than 1  $\mu\text{m}$  and it seems that no change occurs as the solution time increases for Inconel 625 fabricated by DED-LB. This kind of phase was identified through the mapping scanning mode of TEM, and the result is shown in Figure 3(i). It can be seen that this particle phase is rich in Nb and C, but poor in Ni and Cr. Subsequently, the selected area electron diffraction (SAED) spots of this phase were calibrated, indicating that it is the MC-type (Ti, Mo, Nb) C carbide with the same FCC structure. Furthermore, an EDS mapping was conducted on the particle phases near the grain boundaries, as shown in Figure 3(j). The particle is enriched in elements such as Nb and Mo while being deficient in Ni and Cr and it can be determined that these are undissolved Laves phases. This is because the solution temperature was relatively low, and the element diffusion was slow. When Laves phase is dissolved to a certain extent, the concentration gradient became very small, resulting in a slower dissolution rate. The solute release reached equilibrium, and the particle size no longer decreased. Therefore, at the end of the dissolution process, the particle-like phases consist of MC-type carbides and very fine undissolved Laves phases.

## 3.2. High-temperature tensile properties and fracture behaviour

### 3.2.1. Tensile properties at 815°C

Before conducting the high-temperature tensile test, it is necessary to explain the basis for the sampling direction in the mechanical property tests described in this work. According to our previous research on the anisotropy of mechanical properties of nickel-based superalloys, when the loading direction is parallel to the building direction, the alloy exhibits the best strength and plasticity [44]. Wang *et al.* also adopted the method of sampling along the building direction when studying the influence of hot isostatic pressing temperature on the mechanical properties of Hastelloy X alloys [45]. Furthermore, Puskar *et al.* also employed the building direction in their research on the mechanical properties of

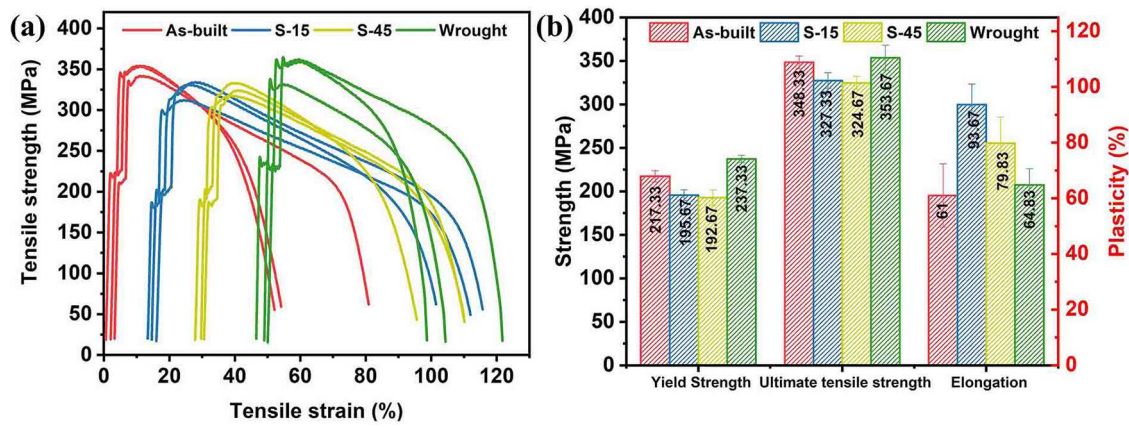
additive manufactured 316L stainless steel [46]. Therefore, the orientation directions of all the mechanical properties specimens are along the building direction.

Figure 5 shows the results of high-temperature tensile tests at 815°C for different heat-treated samples. For each state, a representative curve is selected from the samples and plotted as shown in the Figure 5(a). Subsequently, the average value and standard deviation of the tensile results were calculated, and the results are shown in Figure 5(b). Among them, the yield strength (YS) and ultimate tensile strength (UTS) of the as-built samples were  $217.33 \pm 6.43$  MPa and  $348.33 \pm 7.23$  MPa respectively, with an elongation of approximately 61%. This result is almost comparable to that of the forged piece. Although the tensile properties of the S-15 and S-45 samples were slightly lower than those of the as-built state, especially for the S-45 sample with a UTS of only  $324.67 \pm 7.64$  MPa, it still reached 90% of the forged piece ( $353.67 \pm 14.47$  MPa). This research result provides important reference significance for the laser repair of Inconel 625 alloy. Moreover, the elongation of both the S-15 and S-45 samples exceeded the measured values of the forged parts.

### 3.2.2. Fracture morphology and failure mechanisms

After the tensile test, the tensile fracture surfaces of the Inconel 625 alloy in different states were observed employing SEM and TEM techniques and the results are shown in Figure 6. First, in terms of as-built sample, the elongated Laves phases between the dendrites break down, transforming into short rods or particles after undergoing high-temperature tensile loading, as shown in Figure 6(a). This is because during the deformation process, the elongated Laves phases are not easily able to move with the matrix. The presence of dislocation accumulations around the Laves phases leads to stress concentration, causing the Laves phases to break down. Similarly, some smaller-sized Laves phases exhibit debonding, which is due to the weakened interfacial bonding force between the Laves phases and the matrix under high-temperature conditions. The observation of the fragmentation and debonding of Laves phases in the sample indicates that there is no clear sequence or causal relationship between these two phenomena. In addition, the planes formed by the fragmentation of Laves phases are relatively random. This is because the addition of solute atoms enables the Laves phases to activate more slip systems during the high-temperature tensile process, thus possessing certain plastic deformation capabilities.

The granular Laves phases in S-15 sample exhibited a debonding failure mode in Figure 6(b). Moreover, some



**Figure 5.** High temperature tensile properties of Inconel 625 alloy fabricated by DED-LB and wrought Inconel 625 alloy ( $T = 815^{\circ}\text{C}$ ). (a) Stress-strain curves; (b) the average values of yield strength, ultimate tensile strength and elongation.

larger-sized Laves phases have been detached during mechanical polishing and corrosion processes. For the S-45 sample, since there were still some small particles of Laves phase (less than  $1\ \mu\text{m}$ ) that were not fully dissolved at the grain boundaries before loading, its failure mode was similar to those of the S-15 sample as shown in Figure 6(c). For wrought Inconel 625 alloy, there are a large number of fine MC-type carbides during loading. When the grain boundaries are perpendicular to the stress direction, the amounts of carbides are significantly more than that on the grain boundaries parallel to the stress direction, as shown in Figure 6(d). This phenomenon of stress-induced phase precipitation occurs because the atomic activity intensifies under high-temperature and stress conditions. The stresses on the grain

boundaries in the alloy that are at different angles from the direction of the tensile load are different. The grain boundaries perpendicular to the direction of stress are subjected to tensile stress, while those parallel to the stress direction are subjected to compressive stress. The resulting stress gradient will promote the directional diffusion of vacancies and the diffusion of atoms along the grain boundaries, thereby causing differences in the size and quantity of carbides precipitated at different positions on the grain boundaries.

Further analysis of the as-built sample revealed that a large number of fine  $\gamma''$  phases with a size of approximately 30–50 nm were uniformly distributed near the Laves phase. Similarly, there were also a small number of short rod-shaped  $\delta$  phases with a size of about

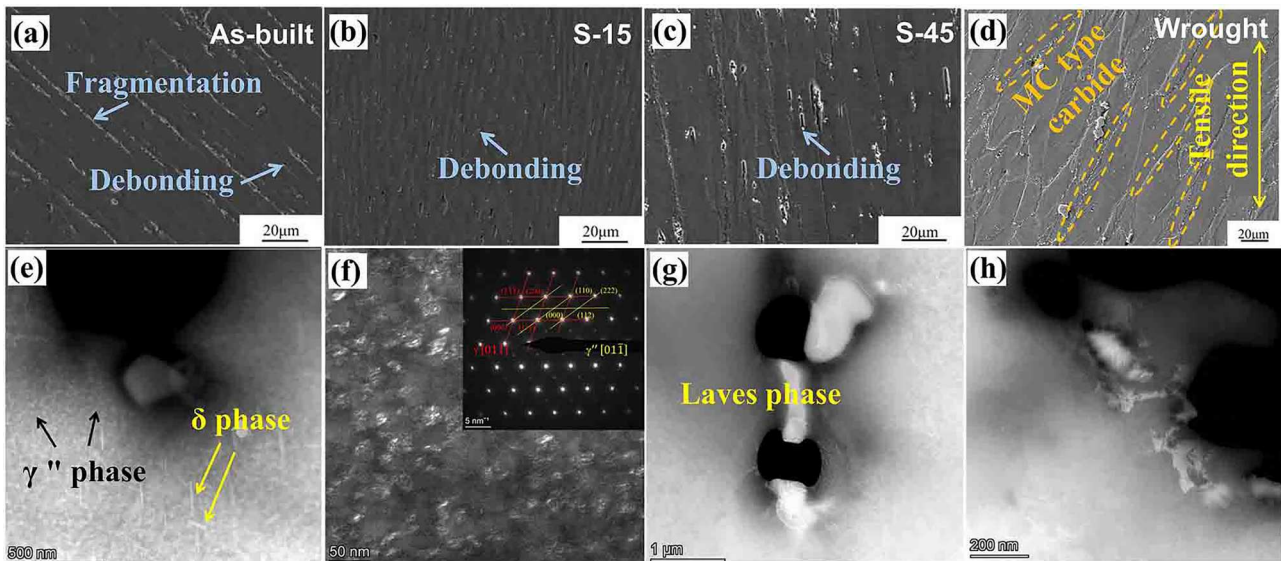


**Figure 6.** Longitudinal cross-section of Inconel 625 specimens in different states at  $815^{\circ}\text{C}$  after tensile fracture. (a) The fragmentation and debonding of the Laves phase in the as-built sample; (b) debonding of Laves phase in S-15 sample; (c) debonding of Laves phase in S-45 sample; (d) MC-type carbides for wrought Inconel 625; (e)  $\gamma''$  phases and  $\delta$  phases in S-15 sample; (f) SAED spot of  $\gamma''$  phase; (g) and (h) no second phase precipitated in the S-15 and S-45 samples.

200 nm, as shown in Figure 6(e). The  $\gamma''$  phase usually precipitates in a coherent manner on the  $\gamma$  matrix and the SAED spots in Figure 6(f) fully confirmed the existence of  $\gamma''$  phase. Since the  $\gamma''$  phase is a metastable phase, it will transform into the equilibrium phase  $\delta$  phase above 650°C [47–49]. The short rod-shaped  $\delta$  phase can also enhance the high-temperature mechanical properties of the alloy. The  $\gamma''$  phase and  $\delta$  phase that precipitate during the high-temperature tensile process are the main reasons for the high strength and low plasticity of the as-built specimen in the high-temperature tensile test. According to the literature, this phenomenon is widespread in nickel-based superalloys. For example, the Inconel 718 alloy also exhibits such characteristics due to the precipitation of  $\gamma''$  phase [50].

However, no precipitated phase was observed near the granular Laves phase in S–15 sample as shown in Figure 6(g). Compared with the S–45 sample, the S–15 sample has higher strength. This phenomenon indicates that the lattice distortion caused by the solidification of elements such as Nb and Mo into the matrix has a relatively small inhibitory effect on dislocations. When these elements exist in the small granular Laves phase, a stress field is generated at the interface between the Laves phase and the matrix, hindering the movement of dislocations. The ability of dislocation pinning is greater than that of solution strengthening. Moreover, due to the small size of the Laves phase particles, they can easily deform along with the matrix, so when the dislocation density at the Laves/ $\gamma$  interface is high, coordinated deformation occurs, allowing dislocations to continue sliding, thereby generating a higher tensile strength. This potential mechanism during the tensile test at 815°C is similar to the strengthening effect of the Laves phase within the Inconel 718 alloy. Also, the Nb element segregation degree near the small-sized Laves phase is relatively low, and no phase transformation occurred during the high-temperature tensile loading, and the microstructure was more stable compared to the as-built sample. Similarly, the precipitated phases at the fracture surface of the S–45 sample were also observed and the result from Figure 6(h) indicates that there was no second phase like  $\gamma''$  phase near the Laves phase. Therefore, S–45 sample is only strengthened by the solution strengthening effect, and its strengthening effect is poor, thus the tensile strength is also the lowest. On the whole, the S–15 sample not only maintained the stability of its microstructure during the high-temperature tensile loading at 815°C, but it also activated the precipitation strengthening effect of the granular Laves phase besides the solution strengthening. The strength reached over 90% of the measured value of the forged piece, and it performed

the best among the three groups of samples combined the strength and plasticity.

### 3.3. Stress rupture properties and strengthening mechanisms

#### 3.3.1. Stress rupture life and elongation

Following the high-temperature tensile test, the stress rupture properties of Inconel 625 alloy with different states were tested and the results are shown in Figure 7. It can be seen that the SR life and elongation of the alloy in all four states meet the requirements of GJB 3317–98 (with a SR life of 23 h and an elongation after fracture of 15%). The SR life of S–45 sample is the lowest, at only 24 h. But its elongation after fracture is the best (147%), which even exceeds the measured value of the forged piece (129%). The SR lives of the as-built and S–15 samples are similar (around 31 h), which have reached 97% of the measured value for the forged piece. Although the elongation of these two is lower than the measured values of the forged parts (147%), they still far exceed the standards for forged parts (15%). In comparison, both the as-built and S–15 samples exhibited better high-temperature SR properties than the S–45 sample.

#### 3.3.2. Fracture morphology after stress rupture

A large number of dimples are evenly distributed in all four samples from Figure 8. Among them, the dimples in the as-built sample and the S–15 sample are smaller, while those in the S–45 sample and the forged piece are larger and deeper. For the as-built sample, the Laves phase has a larger size and is distributed along the grain boundaries. The dimples exhibit obvious dendritic characteristics, and is relatively shallow as shown in Figure 8(a). After the S–15 sample undergoes solution treatment, the Laves phase still distributes along the grain boundaries, but due to the reduction in its

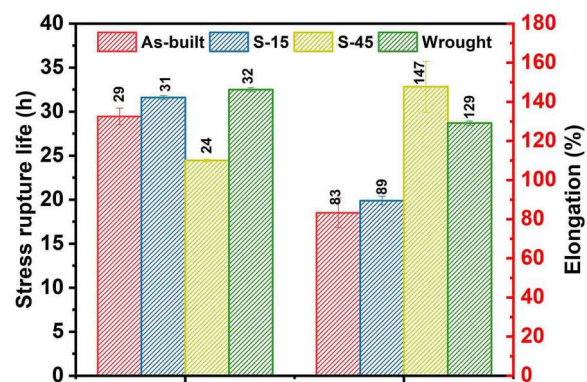
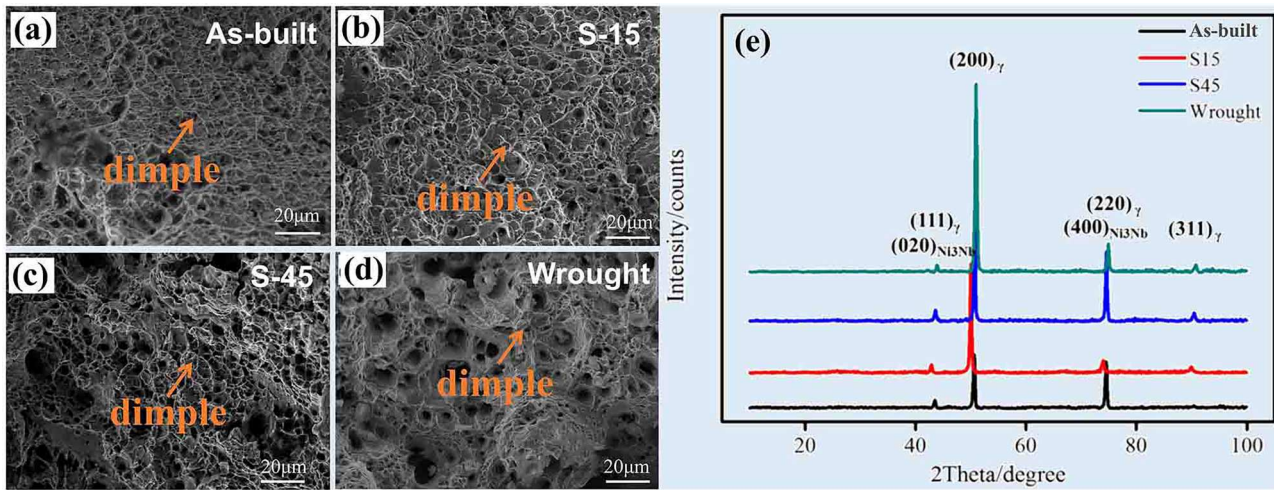


Figure 7. The stress rupture properties of Inconel 625 alloy with different states ( $T = 815^{\circ}\text{C}$ ,  $\sigma = 114 \text{ MPa}$ )



**Figure 8.** Fracture morphology and component analysis of Inconel 625 alloy with different states after stress rupture test. (a) as-built; (b) S-15 sample; (c) S-45 sample; (d) wrought sample; (e) XRD results of longitudinal section of fracture.

volume fraction and the decrease in its size, the dimples are larger and deeper compared to the as-built sample, and no obvious dendritic characteristics are found in Figure 8(b). While the S-45 sample and the forged piece have undergone significant plastic deformation, the dimples take on a larger and deeper shape, as shown in Figure 8(c) and (d). Overall, whether considering the different heat-treated states or the forged Inconel 625 alloy, their fracture patterns are all typical of ductile fracture. Furthermore, the composition of the phases on the fracture surface was analyzed using X-ray diffraction patterns, and the results are shown in Figure 8(e). The composition of the fracture surface was found to be mainly  $\gamma$  phase and possibly  $\delta$  phase. However, no diffraction peaks of Laves phase were detected through peak detection. After speculation, it was believed that the content of Laves phase in the sample was not high, or it might have been affected by the orientation of  $\gamma$  phase, resulting in the weak intensity of a small amount of Laves phase diffraction peaks and their being overlooked. Additionally, since the peaks of  $\delta$  phase were small and overlapped with those of the base  $\gamma$  phase, the formation of  $\delta$  phase could not be completely confirmed. The post-fracture microstructure evolution at high temperatures still needs to be further confirmed by combining subsequent SEM and TEM.

Further observations were conducted on the longitudinal sections of the Inconel 625 alloy in different states, and the results are shown in Figure 9. Whether it is the long-striped Laves phase of as-built sample in Figure 9(a) or the granular Laves phase of S-15 or S-45 samples in Figure 9(d) or (g), the failure of the Inconel 625 alloy is manifested as the debonding of the Laves phase. Studies have shown that the failure mode of

Laves phase is characterised by debonding that is positively correlated with temperature and fragmentation that is positively correlated with stress level [51]. Since the loading environment in this work is at a high-temperature and low-stress level (815°C/114 MPa), the fracture mechanism of the alloy is mainly the debonding between the Laves phase and the matrix. This is because at high temperatures, the interfacial bonding force of the Laves phase weakens, causing the Laves phase and the matrix to debond, resulting in the aggregation of micro-pores and triggering the fracture.

In addition to the debonding of the Laves phase, the precipitation of the second phase was also observed. In terms of as-built state, a large number of short rod-shaped and fine needle-shaped precipitated phases are distributed around the long-striped Laves phase, as shown in Figure 9(b) and (c). In the S-15 sample, similar precipitated phases are also distributed around the granular Laves phase, as shown in Figure 9(e). However, compared with the as-built sample, this second phase is much finer, as shown in Figure 9(f). After phase identification, it was found that this phase is actually  $\delta$  phase and this is elaborated in detail in Section 3.3.3. In the S-45 sample, the post-fracture microstructure shows a small amount of granular carbides or undissolved, very fine Laves phase and short rod-shaped  $\delta$  phases at the grain boundaries and in some original dendritic regions, as shown in Figure 9(g). The volume fraction of  $\delta$  phases is much lower than that of the as-built sample and S-15 sample from Figure 9(h) and (i). This is because, after a long period of solution treatment, the Nb element homogenisation has improved, making it difficult to reach the critical condition for  $\delta$  phase precipitation. Only near a few large undissolved particles can this requirement be met.

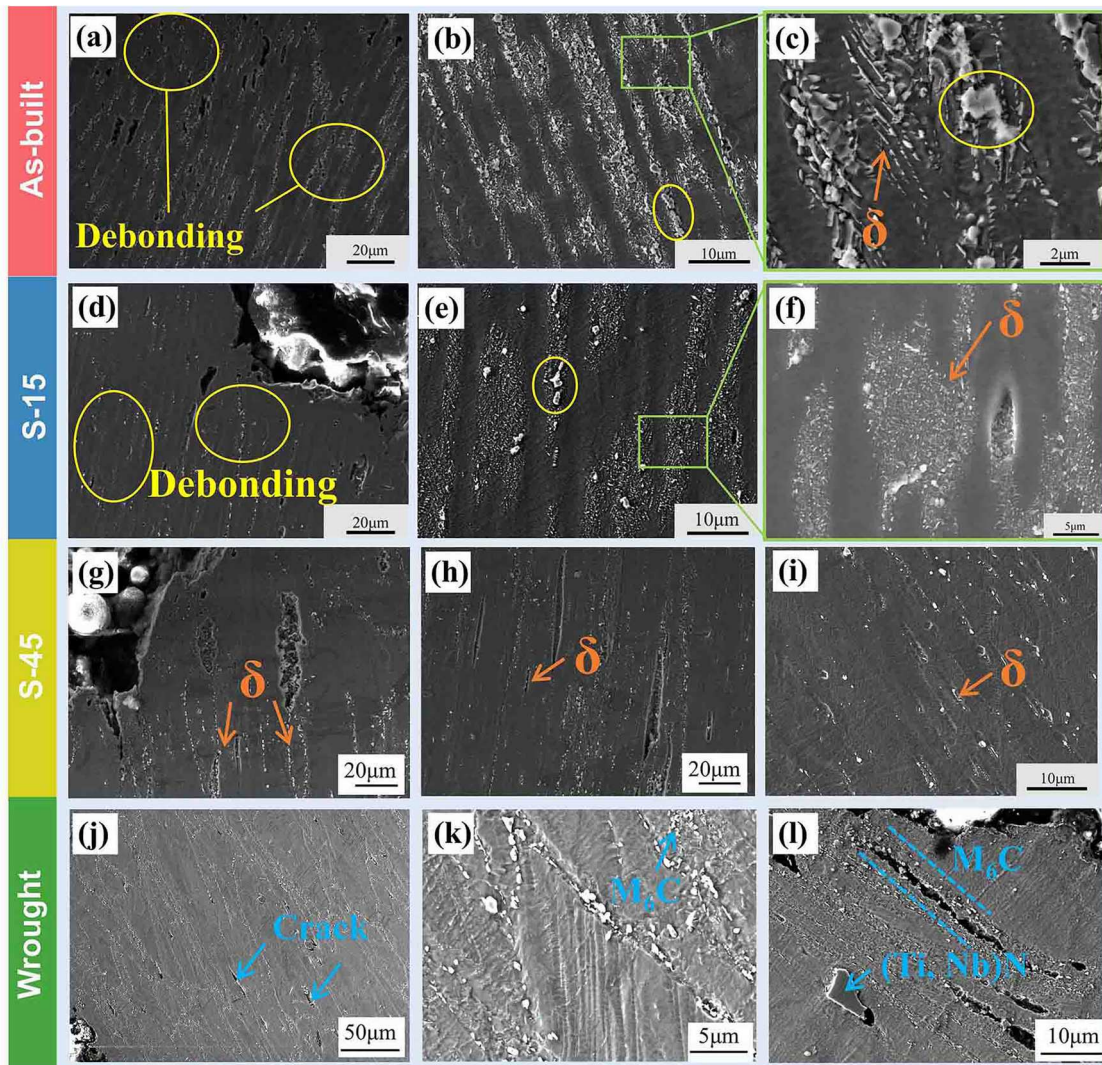


**Figure 9.** The longitudinal fracture morphology of Inconel 625 alloy with different states after stress rupture test. (a–c) as-built; (d–f) S–15 sample; (g–i) S–45 sample; (j–l) wrought sample.

In contrast, a large number of cracks running along the grain boundaries are distributed on the fracture surface of the forgings as shown in Figure 9(j). This indicates that the grain boundaries are not only the channels for crack initiation but also can hinder their further expansion. This is attributed to the large number of fine granular precipitates at the grain boundaries, which can effectively pin the grain boundaries when dislocations move to the grain boundaries, thereby playing a strengthening role. The size of this granular phase is smaller than that of the MC-type carbides before loading, approximately 0.2–0.5  $\mu\text{m}$ , and some of the particles are interconnected as shown in Figure 9(k). Table 5 shows the EDS results of this granular phase. After analysis, this granular phase is of the  $M_6C$  type carbide. In addition, the large black nitrides also exhibit a debonding failure mode under local stress concentration from Figure 9(l).

**Table 5.** Transmission EDS results of granular phase of wrought after stress rupture.

| Element             | C     | Cr   | Fe   | Ni    | Nb   | Mo   |
|---------------------|-------|------|------|-------|------|------|
| Atomic fraction (%) | 14.97 | 8.69 | 1.54 | 61.1  | 9.75 | 3.96 |
| Mass fraction (%)   | 3.22  | 8.08 | 1.54 | 64.17 | 16.2 | 6.79 |

### 3.3.3. Influence of precipitation phases on rupture behaviour

The  $\delta$  phase generated during the high-temperature SR process was further confirmed by means of TEM technology combined with the lattice constant of  $\delta$  phase and the result is shown in Figure 10(a). From the analysis of scanning transmission electron microscope (STEM) data of Figure 10(b), it can be observed that the precipitation of  $\delta$  phase is mainly dependent on the Laves phase. The EDS line scan results for Ni and Nb elements were conducted, and the scanning positions are

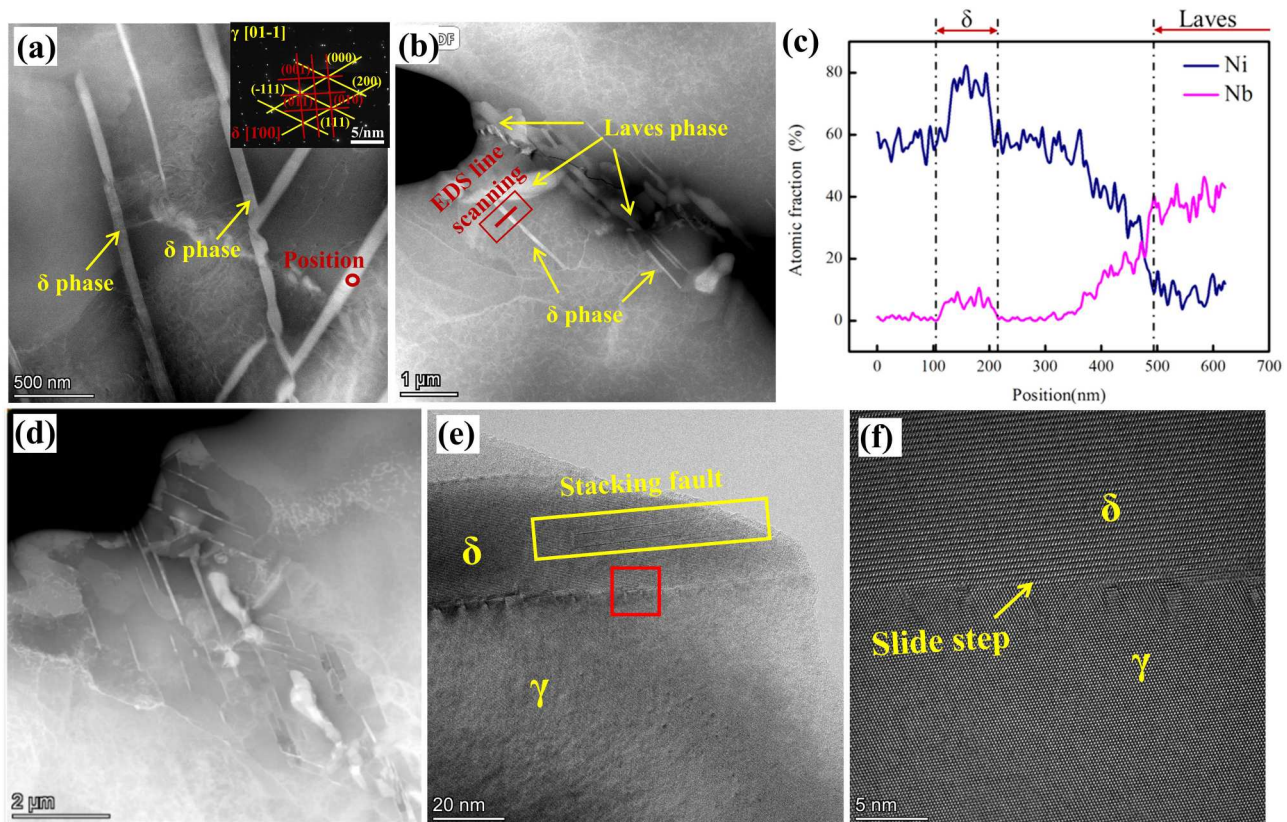


**Figure 10.** The longitudinal fracture morphology of Inconel 625 alloy with different states after stress rupture test. (a–c) as-built; (d–f) S–15 sample; (g–i) S–45 sample; (j–l) wrought sample.

indicated by the red frame in Figure 10(b). The element distribution results are shown in Figure 10(c). The Nb element enriched in the Laves phase provides the necessary conditions for the formation of the  $\delta$  phase, while the Ni element required for the growth of the  $\delta$  phase is obtained from the  $\gamma$  matrix.

In addition, by comparing the microstructures of the as-built and S–15 sample after loading, it can be observed that the  $\delta$  phase in the as-built sample has a larger size and a higher content. The volume fraction of the  $\delta$  phase after statistics is approximately 14%, with a length of more than 2  $\mu\text{m}$ . In contrast, the  $\delta$  phase content in the S–15 sample is about 8%, and its morphology is mostly short rod-shaped, with a length of less than 1  $\mu\text{m}$ . This is due to the fact that before loading, there were more Laves/ $\gamma$  interfaces in the as-built sample, and the Nb element segregation level was also relatively high. Furthermore, the low-magnification microstructure observation of the as-built sample also revealed that some of the elongated Laves phases in the as-built or S–15 sample had partially dissolved, as shown in the yellow circles in Figure 9(b) and (e). This is because the precipitation of  $\delta$  phase requires a relatively high amount of Nb, so some Nb elements can only be replenished from the Laves phases that are enriched in Nb [52], which also

provides evidence for the non-uniform precipitation of the  $\delta$  phase. Table 6 presents the volume fraction of Laves phase and the content of Nb element in the matrix after high-temperature long-term loading. Compared with Tables 4 and 6, the decrease in the volume fraction of Laves phase and the increase in the content of Nb element in the matrix are evidence of the transformation of Laves phase to  $\delta$  phase. Compared with the current reports, whether it is the Inconel 625 alloy or the Inconel 718 alloy, the common phenomenon is the transformation from  $\gamma'$  to  $\delta$  phase during the high temperature loading process [53–55], and the transformation from Laves phase to  $\delta$  phase is rarely observed due to the complete dissolution of the Laves phase. Therefore, it is an interesting phenomenon in this work.

After clarifying the generation of  $\delta$  phase, a further analysis was conducted on the influence of Laves phase

**Table 6.** Statistics of Laves phase volume fraction and Nb element content in matrix of sample S0 and sample S15 after stress rupture.

| Sample   | The volume fraction of Laves phase | Mass fraction of Nb element in $\gamma$ matrix |
|----------|------------------------------------|--|
| As-built | 3.93 vol%                          | 1.79 wt%                                       |
| S15      | 0.77 vol%                          | 2.60 wt%                                       |

and  $\delta$  phase on the high-temperature SR properties of the alloy. The influence of  $\delta$  on mechanical properties mainly manifests in two aspects. Firstly, the precipitation of the  $\delta$  phase consumes a large amount of Nb element [56], causing the long-stripped Laves phase to dissolve and break before loading, resulting in a reduction in size and the formation of some fragmented Laves phases with lengths concentrated around  $2\ \mu\text{m}$ , as shown in the yellow circle of Figure 9(c). The Laves phase and the  $\delta$  phase for the as-built samples will undergo an obviously new dynamic size matching during the loading process. After loading, the size of some Laves phases is similar to the size of granular Laves phases in the S-15 sample, thus further improving the strengthening effect of the Laves phase. Secondly, a large number of short rod-shaped  $\delta$  phases precipitated around the Laves phase makes it less likely to cause stress concentration when subjected to the same stress level due to the increased number of interfaces. Moreover, the  $\delta$  phases around the Laves phase can prevent dislocations from moving to the interface between the Laves phase and the  $\gamma$  matrix, which reduces the local stress at the Laves/ $\gamma$  interface and lowers the probability of Laves phase debonding, thus achieving a high SR life. This was also discovered by Liu *et al.* in laser-directed energy deposited Inconel 718 alloy [52]. Figure 10(d) shows the transmission micrograph of the region near the dendrites after loading. It can be seen that the Laves phase between the dendrites is surrounded by the precipitated  $\delta$  phase. The dislocation lines near the Laves phase are less distributed. The dislocation density gradually increases from the Laves phase to the surrounding  $\delta$  phase, and it is already very high in the matrix, with phenomena such as dislocation entanglement even occurring. The dislocations near the  $\delta$  phase are further magnified as shown in Figure 10(e), and the interface between the  $\delta$  phase and the  $\gamma$  matrix can be clearly observed, as shown in the red box. When the red box region is magnified, it can be observed from Figure 10(f) that when the dislocation moves to the edge of the  $\delta$  phase and is cut, it forms a slip step. This causes some atomic misalignment, increasing the interfacial energy, thereby creating a significant obstacle to the movement of the dislocation.

Although the precipitation of  $\delta$  phase is beneficial for improving the SR life, conversely, the  $\delta$  phase is distributed near the Laves phase in the dendrites, resulting in a shorter dislocation slip distance. Moreover, the Laves phase and  $\delta$  phase clusters are not easily moved along with the matrix, thus causing poor elongation of the alloy. Eventually, the crack initiates at the interface between the Laves phase and the matrix and then breaks. However, in the S-45 sample, due to the significant reduction in the degree of Nb element segregation,

the Nb element in the alloy is mostly below 6 wt. %, so except for the precipitation of a small number of fine short rod-shaped  $\delta$  phases at some grain boundaries, no  $\delta$  phase appears within the grains. This is the reason why the elongation of the S-45 sample is better than that of the as-built state and S-15 sample.

The microstructures of the S-45 sample and forged piece are similar, both mainly consisting of the  $\gamma$  matrix and a small amount of smaller-sized secondary phases. Among them, the granular Laves phases and carbides in the S-45 mainly distribute at the grain boundaries, and a very small amount of  $\delta$  phases is precipitated during the high-temperature loading process. Before loading, the forged piece mainly has MC-type carbides distributed at the grain boundaries, and after loading, it mainly has smaller-sized  $M_6C$ -type carbides. However, there is a significant difference in the high-temperature SR life of the two samples. Therefore, comparing their microstructures can reveal the influence of carbides on the high-temperature SR properties of the alloy.

The high-temperature SR properties of the S-45 sample are characterised by a relatively low SR life and excellent elongation after fracture. This is related to its microstructure features before loading. Due to the long slip path of dislocations in the solution state, the only thing that can hinder the movement of dislocations is distorted lattices. Therefore, its SR life is relatively low. After loading, the phase of the S-45 sample transforms to a small amount of  $\delta$  phase appears at the grain boundaries. According to the aforementioned analysis, since the Nb element segregation condition of the alloy has been significantly reduced after a long period of solution treatment, it fails to meet the elemental conditions required for the formation of  $\delta$  phase, so the size and volume fraction of  $\delta$  phase are at a relatively low level. Therefore, when dislocations accumulate at the grain boundaries, cracks will initiate at the grain boundaries, which ultimately leads to the failure of the sample. This result also precisely addresses the current controversy regarding whether the  $\delta$  phase has a strengthening or deteriorating effect on the high-temperature properties of nickel-based superalloys [57–59]. That is to say, only when the dimensions and volume fraction of the  $\delta$  phase are within a reasonable range can its strengthening effect on mechanical properties be fully exerted.

The high-temperature SR properties of the forgings are excellent, with both the SR life and the elongation after fracture being relatively high. This is because the grains of the forgings are fine, and the carbides distributed on the grain boundaries act as a reinforcement, resulting in the fine-grain strengthening effect in terms of blocking the movement of dislocations and coordinating deformation. It is noted that the size of the MC-type carbides

distributed on the grain boundaries before loading was relatively large, approximately 2  $\mu\text{m}$ . After high-temperature loading, the  $\text{M}_6\text{C}$  appeared as fine granular and discontinuously distributed on the grain boundaries. This is because the primary MC is unstable, and it will undergo different degrees of degradation reactions with changes in time and temperature under high-temperature long-term holding, possibly forming decomposition products such as  $\text{M}_6\text{C}$  or  $\text{M}_{23}\text{C}_6$  [60]. The fine granular  $\text{M}_6\text{C}$  formed has a reinforcement impact on the high-temperature SR properties of the alloy. It has a significant interaction with dislocations and effectively hinders the movement of dislocations and grain boundaries through pinning, and there are few cracks at the interface between the matrix and  $\text{M}_6\text{C}$ . In addition to the dispersion strengthening effect, another notable feature of the forging microstructure is the twinning shown in Figure 4(d) and (h). During high-temperature loading, twinning can simultaneously improve both strength and plasticity [61–63], which also contributes to the excellent stress rupture life of the forging.

### 3.3.4. Role of dynamic recovery during stress rupture

Apart from the influence of the precipitation phase, dynamic softening is also an important factor affecting the high-temperature properties of the alloy. Figure 11 shows the grain characteristics of the Inconel 625 alloy in three states before and after high-temperature long-term loading. Before the high-temperature loading, all of the as-built, S–15 and S–45 samples were mainly composed of large and coarser columnar grain, and the sizes of the grains were not significantly different, shown in Figure 11(a–c). In contrast, after the high-temperature loading was completed, it could be observed from Figure 11(d–f) that the columnar grains were significantly elongated along the loading direction, and many small-angle grain boundaries were also generated.

After a preliminary understanding of the evolution of grain morphology before and after loading, it is well known that alloys will experience the accumulation of dislocations during high-temperature deformation. When the dislocation density in the alloy increases to a certain extent, and under appropriate deformation temperature and strain rate conditions, dynamic softening will occur. For instance, *Hu et al.* observed the dynamic recrystallisation during the high-temperature deformation process of laser directed energy deposited Inconel 625 alloy [64]. Figure 11(g–i) shows the EBSD maps of Inconel 625 alloy with different states before and after high-temperature long-term loading in this work. Among them, blue represents recrystallised grains, yellow represents substructured grains, and red

represents deformed grains. It can be seen that in the three different states, the recrystallisation volume fraction of Inconel 625 alloy is all relatively small after fracture.

Compared with the work from *Hu et al.*, although no dynamic recrystallisation occurred in the alloy before and after loading, it can be determined from Figure 10 that the contents of high-angle grain boundaries (HAGBs, more than  $15^\circ$ ), medium-angle grain boundaries (MAGBs,  $2\text{--}15^\circ$ ), and low-angle grain boundaries (LAGBs, less than  $2^\circ$ ) have all undergone significant changes [65]. Figure 12(a–c) quantitatively presents the volume fractions of HAGBs, MAGBs, and LAGBs of the Inconel 625 alloy before and after loading. It can be seen from Figure 12(a) that for the as-built state, the volume fraction of HAGBs decreases from 80.67% to 36.66%, MAGBs increase from 15.9% to 53.02%, and LAGBs increase from 3.43% to 10.32%. Correspondingly, in the S–15 sample of Figure 12(b), HAGBs decrease from 86.82% to 43.99%, MAGBs increase from 12.55% to 44.55%, and LAGBs increase from 0.63% to 11.56%. In the S–45 sample of Figure 12(c), HAGBs decrease from 85.31% to 56.81%, MAGBs increase from 13.3% to 32.41%, and LAGBs increase from 1.39% to 10.78%. According to the above statistical results, the HAGBs content is decreasing, while both the MAGBs and LAGBs are increasing for the three types of samples. Especially in the as-built state and S–15 sample, the increases of MAGBs and LAGBs are more significant. It is well known that dynamic recovery is one of the main mechanisms of dynamic softening [66,67]. This process is mainly characterised by the movement and change of dislocations, and is manifested as the formation of dislocation cells – polygonisation – formation of subgrain boundaries. Therefore, the occurrence of dynamic recovery is manifested in the statistical results of local orientation differences as an increase in the number of MAGBs. That is to say, a significant dynamic recovery phenomenon occurred in the as-built state and S–15 sample.

Taking the as-built sample as an example, Figure 12(d–f) shows the TEM image of the dynamic recovery observed in the alloy after high-temperature long-term loading. It can be seen that the dislocation movement is hindered near the  $\delta$  phase and Laves phase, resulting in dislocation pile-up. As the degree of dislocation pile-up and entanglement gradually increases, the larger distortion energy promotes its rearrangement, thereby forming different-sized dislocation cells and dislocation walls, as shown in Figure 12(d). The borders of dislocation cells are composed of a large number of intertwined dislocations, and there are no dislocations or a low dislocation density within the dislocation cells, indicating

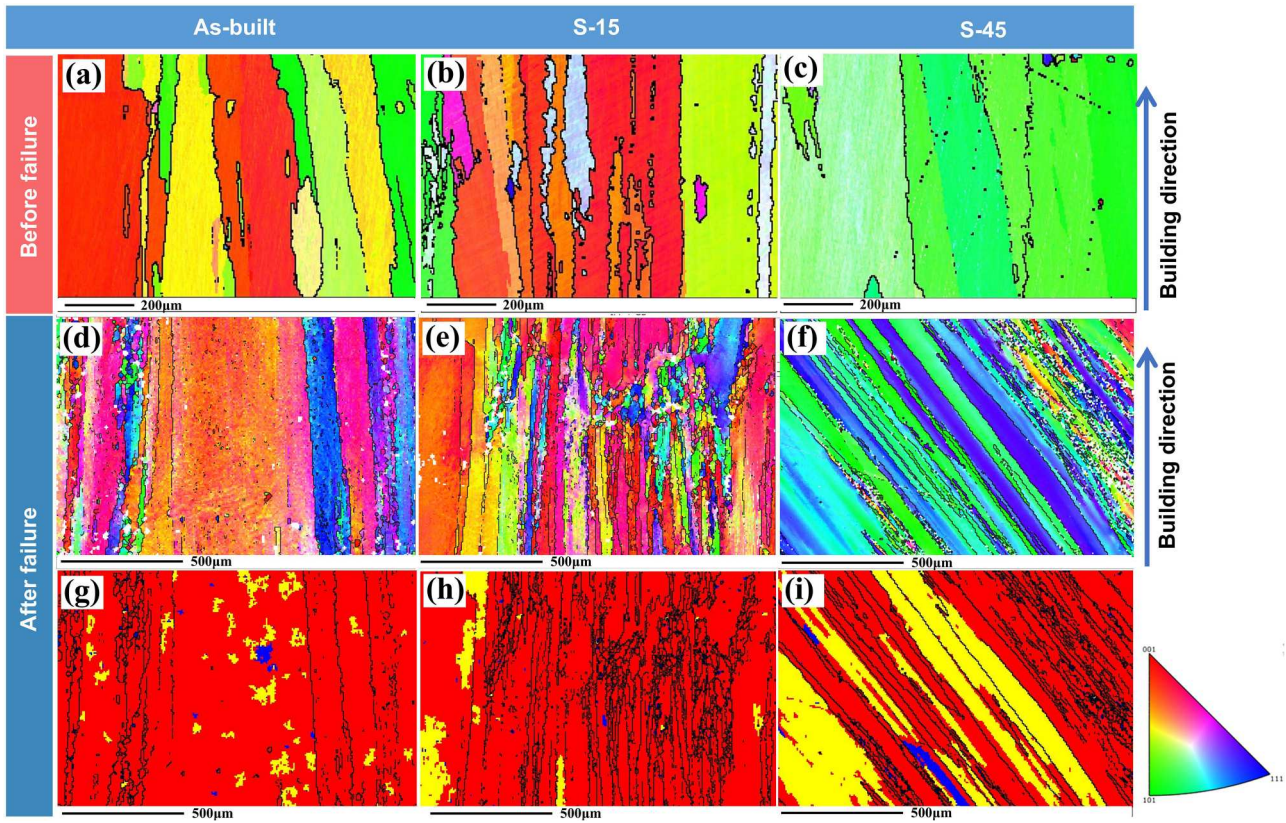


**Figure 11.** The grain characteristics and recrystallisation degree of three different states of IN625 alloy before and after the stress rupture fracture. (a), (b), and (c) the grain morphologies of as-built, S–15, and S–45 samples before the stress rupture fracture; (d), (e), and (f) the grain morphologies after the stress rupture fracture of as-built, S–15, and S–45 samples after the stress rupture fracture; (g), (h), and (i) the recrystallisation degrees after the stress rupture fracture of as-built, S–15, and S–45 samples after the stress rupture fracture.

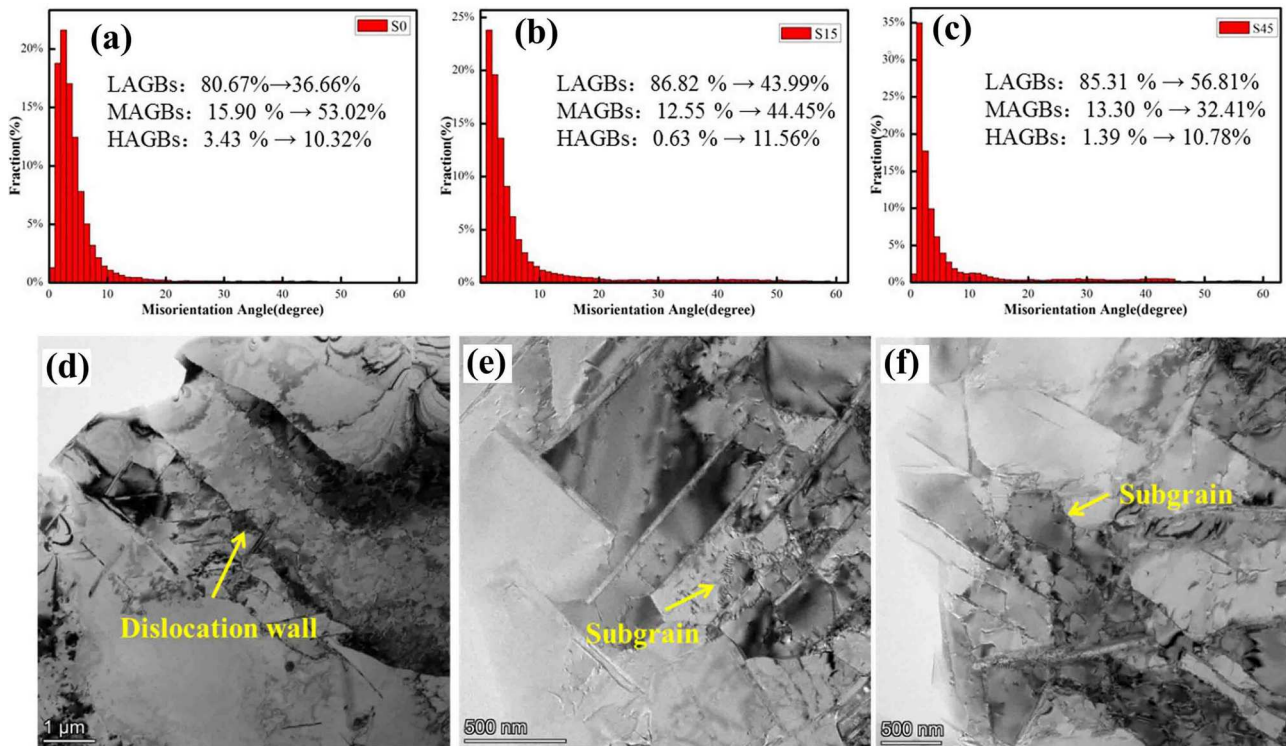


**Figure 12.** The statistical results of the local orientation differences of samples in different states and results of the transmission experiment. (a), (b), and (c) the volume fractions of HAGBs, MAGBs, and LAGBs in as-built, S–15, and S–45 samples; (d) the dislocation wall formed near the  $\delta$  phase; (e) and (f) the subgrains formed near the  $\delta$  phase.

that the dislocation cells have undergone rearrangement and cancellation. The formation of dislocation cells consumes part of the distortion energy, allowing the deformation to continue. Compared to straight dislocation rows, the storage energy of the disordered dislocation network is higher, so dislocation movement such as sliding and sliding will occur or dislocation reactions will be promoted, reducing the dislocation density, or rearranging them to become straight, thus forming subgrains with larger curvature boundaries, as shown in Figure 12(e) and (f). Therefore, there are more MAGBs larger than  $2^\circ$ . In addition, it can be found that most straight dislocation rows are distributed on the  $\delta$  phase, as shown in Figure 12(f). From Figure 12, it can be seen that in both the as-built sample and the S-15 sample, a large amount of  $\delta$  phase was precipitated near the Laves phase, which provided favourable conditions for the accumulation of dislocations. During the high-temperature SR process, this would promote the occurrence of dynamic recovery, thus resulting in a longer high-temperature SR life. However, in the S-45 sample, the dislocation slip distance was long, and only the boundaries of the straight columnar grains provided the accumulation site for dislocations. Therefore, the degree of dynamic recovery was lower, and it was manifested as a higher elongation rate and a lower SR life.

By comprehensively comparing the high-temperature tensile and SR properties of the three groups of specimens, it was found that the high-temperature tensile performance of the S-15 specimen was superior to that of the S-45 specimen, and its microstructure was more stable compared to the as-built specimen. The high-temperature tensile strength also reached over 90% of the measured value of the forging. Moreover, the high-temperature SR life of S-15 specimen was significantly better than that of the S-45 specimen, capable of withstanding a greater endurance load and achieving a SR life of over 95% of the measured value of the forging. The high-temperature comprehensive properties of the S-15 specimen are excellent, providing certain reference significance for the laser repair of Inconel 625 alloy.

#### 4. Conclusions

This work is primarily aimed at boosting the high-temperature mechanical properties of laser-directed energy-deposited Inconel 625 alloy; through adjusting the post-heat treatment, the Laves phases with different morphologies, sizes, and volume fractions were acquired. The high-temperature tensile properties and stress rupture life at 815°C of Inconel 625 alloy, retaining the Laves phase with different characteristic parameters,

were investigated. Furthermore, the influence mechanism of Laves phases on the high-temperature tensile and stress rupture life was unveiled systematically. The main conclusions of the study were as follows:

- (1) Grains and precipitated phases of Inconel 625 alloy after different heat treatment regimes were characterised. Whether it is the as-built or heat-treated samples, all of the microstructures were mainly composed of coarse columnar grains. The main differences were reflected in the morphology and volume fraction of the Laves phase. The as-built samples mainly consisted of long-striped Laves phases, with a volume fraction of approximately 13.2%. When the solution time was extended to 15 min, the morphology of Laves phase dissolved to a granular form, and the content rapidly decreased to 1.2%. When the time was 45 min, there were only a very small number of undissolved granular Laves phases.
- (2) High-temperature mechanical properties of Inconel 625 alloy with different states were tested repeatedly. As the solution time was extended from 0 min to 45 min, the yield strength of Inconel 625 alloy decreased from 217.33 MPa to 192.67 MPa at 815°C, and the tensile strength dropped from 348.33 MPa to 324.67 MPa. In terms of elongation rate, when the solution time is 15 min, the elongation rate of the alloy reaches its maximum, approximately 93.67%. In addition, the stress rupture tests indicated that when the solution time is 0 and 15 min, the stress rupture life of the alloy can be compared to the measured values of the forgings. However, the stress rupture life was obviously lower than that of the forgings when the time extends to 45 min.
- (3) Underlying mechanism of Inconel 625 alloy after the high-temperature tensile test was elucidated. For the as-built state, the failure of the alloy manifested as the fragmentation and debonding of the Laves phase; as the Laves phase was dissolved, the failure of the alloy mainly reflected in the debonding of the Laves phase. Moreover, the excellent tensile strength was attributed to the uniform precipitation of the  $\gamma'$  phase and some  $\delta$  phase near the Laves phase for the as-built Inconel 625 alloy. When the solution time was 15 min, the constraint effect of Laves/ $\gamma$  on dislocations improved the strength and ductility of the alloy. The low strength and high plasticity characteristics were the result of the  $\gamma$  solid solution structure with long dislocation slip paths when the solution time is 45 min.
- (4) Influence of precipitation phase and grain on stress rupture behaviour of Inconel 625 alloy was clarified.

In both cases of 0 and 15 min, the Inconel 625 alloy exhibited outstanding stress rupture life because a certain content of  $\delta$  phases was precipitated around the Laves phase, hindering dislocation movement and promoting the dynamic recovery process, resulting in a longer SR life. On the contrary, due to the fact that it has very few  $\delta$  phases when the solution time is 45 min, it leading to a poorest stress rupture life. It is worth noting that dynamic recovery is also a key factor influencing the stress rupture life. At 45 min, the lowest dynamic recovery degree of the alloy is also the primary reason for the poorest stress rupture life.

## Acknowledgements

Zuo Li (First author): Writing-Original Draft, Writing-Review & Editing; Xin Lin (Corresponding author): Conceptualisation, Supervision, Funding Acquisition; Xin Hou: Resources, Investigation; Zhiwei Hao: Formal analysis, Investigation; Wei Fan: Methodology, Validation; Chongliang Zhong: Validation, Visualisation; Hua Tan: Funding Acquisition, Validation; Yiyi Zhou (Corresponding author): Methodology, Supervision; Yi Min Xie: Validation, Formal Analysis.

## Author contributions

CRedit: **Zuo Li**: Writing – original draft, Writing – review & editing; **Xin Lin**: Conceptualization, Funding acquisition, Supervision; **Xin Hou**: Investigation, Resources; **Zhiwei Hao**: Formal analysis, Investigation; **Wei Fan**: Methodology, Validation; **Chongliang Zhong**: Validation, Visualization; **Hua Tan**: Funding acquisition, Validation; **Yiyi Zhou**: Methodology, Supervision; **Yi Min Xie**: Formal analysis, Validation.

## Disclosure statement

No potential conflict of interest was reported by the author(s).

## Funding

This work was supported by the National Natural Science Foundation of China [grant numbers 52505369, U22A20189 and 52175364], Changzhou City Science and Technology Project–Applied Basic Research [grant number CJ20250105].

## Data availability

All data included in this study are available upon request by contact with the corresponding author. The data that support the findings of this study are openly available at <https://doi.org/10.6084/m9.figshare.30434638>.

## References

- [1] Wang K, Yi Z, Song Z, et al. Wear behaviors of laser-directed energy deposited Inconel 625 alloys-based composite coating by different oscillating laser paths. *Opt Laser Technol.* 2025;192:113900.
- [2] Cao K, Fan J, Liu X, et al. Microstructure and mechanical properties of nickel-based wrought superalloys under thermal-mechanical coupling: a review with Inconel 718, 625 as main cases. *Prog Nat Sci Mater Int.* 2025;35(1):65–82.
- [3] An Z, Pan J, Hu X, et al. Analysis of melt pool evolution, defect mechanisms, and grain growth of Inconel 625 formers in selective laser melting. *Int J Heat Mass Transfer.* 2025;238:126452.
- [4] Mostafaei A, Toman J, Stevens EL, et al. Microstructural evolution and mechanical properties of differently heat-treated binder jet printed samples from gas- and water-atomized alloy 625 powders. *Acta Mater.* 2017;124:280–289.
- [5] Chaurasia JK, Jinoop AN, Paul CP, et al. Effect of deposition strategy and post processing on microstructure and mechanical properties of serviced Inconel 625 parts repaired using laser directed energy deposition. *Opt Laser Technol.* 2024;168:109831.
- [6] Sui S, Li H, Li Z, et al. Introduction of a new method for regulating laves phases in Inconel 718 superalloy during a laser-repairing process. *Engineering.* 2022;16:239–246.
- [7] Liu M, Cai Y, Duan C, et al. Key techniques in parts repair and remanufacturing based on laser cladding: a review. *Mater Manuf Processes.* 2024;132:994–1014.
- [8] Li Y, Lin X, Hu Y, et al. Microstructure and fracture toughness of a Nb–Ti–Si-based in-situ composite fabricated by laser-based directed energy deposition. *Compos B Eng.* 2024;278:111427.
- [9] Li Z, Sui S, Ma X, et al. High deposition rate powder- and wire-based laser directed energy deposition of metallic materials: a review. *Int J Mach Tools Manuf.* 2022;181:103942.
- [10] Song W, Wang D, Tang C, et al. Effects of added tungsten on the microstructure and mechanical properties of laser-directed energy deposited Inconel 625 alloys. *Mater Sci Eng A.* 2023;883:145481.
- [11] Kim C, Yang C-H, Kong B-O, et al. Comparative analysis of microstructure and creep properties in cast Inconel 625 welds fabricated by gas tungsten and shielded metal arc welding processes. *Mater Sci Eng A.* 2024;894:146189.
- [12] Vats P, Khanna N, Kumar A, et al. Tribological performance of hBN and graphene-enriched hybrid nanofluids on tool wear and hole surface quality in drilling: a comparative study on WAAM and wrought Inconel 625. *Wear.* 2025;574-575:206090.
- [13] Chaudhuri A, Raghupathy Y, Srinivasan D, et al. Microstructural evolution of cold-sprayed Inconel 625 superalloy coatings on low alloy steel substrate. *Acta Mater.* 2017;129:11–25.
- [14] Ding Y, Gui W, Nie B, et al. Elimination of elemental segregation by high-speed laser remelting for ultra-high-speed laser cladding of Inconel 625 coatings. *J Mater Res Technol.* 2023;24:4118–4129.
- [15] Lin X, Yang D, Gu X, et al. Enhancement of mechanical properties and corrosion resistance of wire-arc directed energy deposited thin-walled Inconel 625 via post heat treatment. *Mater Today Commun.* 2025;49:113672.
- [16] Farias FWC, Duarte VR, Felice IO, et al. In situ interlayer hot forging arc-based directed energy deposition of Inconel®

- 625: process development and microstructure effects. *Add Manuf.* **2023**;66:103476.
- [17] Mishra R, Pandit D, Imam M. Microstructure, mechanical and corrosion study of friction stir processed Inconel 625 additive layers deposited via wire arc direct energy deposition. *Add Manuf.* **2024**;86:104193.
- [18] Mostafaei A, Ghiaasiaan R, Ho IT, et al. Additive manufacturing of nickel-based superalloys: a state-of-the-art review on process-structure-defect-property relationship. *Prog Mater Sci.* **2023**;136:101108.
- [19] Lee JS, Armaki HG, Maruyama K, et al. Causes of breakdown of creep strength in 9Cr–1.8W–0.5Mo–VNb steel. *Mater Sci Eng A.* **2006**;428(1):270–275.
- [20] Choudhary BK. Microstructural degradation and development of damage during creep in 9% chromium ferritic steels. *Trans Indian Inst Met.* **2016**;69(2):189–195.
- [21] Wu G, Ding K, Qiao S, et al. Weakening modes for the heat affected zone in Inconel 625 superalloy welded joints under different high temperature rupture conditions. *J Mater Res Technol.* **2021**;14:2233–2242.
- [22] Marchese G, Lorusso M, Parizia S, et al. Influence of heat treatments on microstructure evolution and mechanical properties of Inconel 625 processed by laser powder bed fusion. *Mater Sci Eng A.* **2018**;729:64–75.
- [23] Proehl ER, Zhong W, Sprouster DJ, et al. Effect of stress on Laves phase precipitation in creep ruptured Grade 92 ferritic martensitic steel characterized by a novel accessible method. *Acta Mater.* **2025**;301:121559.
- [24] Sui S, Tan H, Chen J, et al. The influence of Laves phases on the room temperature tensile properties of Inconel 718 fabricated by powder feeding laser additive manufacturing. *Acta Mater.* **2019**;164:413–427.
- [25] Li Z, Lin X, Tan H, et al. Multi-scale microstructure and its synergetic strengthening effect in stress rupture life of Inconel 718 fabricated by high-deposition-rate laser directed energy deposition. *Mater Sci Eng A.* **2024**;915:147211.
- [26] Long W, Liu B, Cao Y, et al. Exceptional elevated-temperature properties of a Laves phase-strengthened CoNiCrFe high-entropy alloy. *Mater Sci Eng A.* **2024**;916:147366.
- [27] Liu H, Wei L, Ma M, et al. Laves phase precipitation behavior and high-temperature strength of W-containing ferritic stainless steels. *J Mater Res Technol.* **2020**;9(2):2127–2135.
- [28] Li K, Ren Y, Xie G, et al. Effect of solid-solution treatment on high-temperature properties and creep fracture mechanism of laser powder bed fused Inconel 625 alloy. *Mater Sci Eng A.* **2024**;902:146592.
- [29] An Z, Pan J, Han Z, et al. Microstructure and anisotropic mechanical properties of selective laser melted Inconel 625 with heat treatment regulation. *Mater Sci Eng A.* **2025**;943:148830.
- [30] Pasiowiec H, Dubiel B, Dziurka R, et al. Effect of creep deformation on the microstructure evolution of Inconel 625 nickel-based superalloy additively manufactured by laser powder bed fusion. *Mater Sci Eng A.* **2023**;887:145742.
- [31] Kim K-S, Kang T-H, Kassner ME, et al. High-temperature tensile and high cycle fatigue properties of inconel 625 alloy manufactured by laser powder bed fusion. *Add Manuf.* **2020**;35:101377.
- [32] Zhang S, Wang Y, Lv L, et al. Effect of powder layer thickness on the microstructure and properties of Inconel 625 superalloy manufactured by selective laser melting. *J Alloys Compd.* **2025**;1020:179465.
- [33] Shankar V, Kumar H, Kannan R, et al. Studies on high-temperature fatigue behaviour and mechanism for conventionally cast and directed energy deposited forms of Alloy 625. *Int J Fatigue.* **2024**;178:108005.
- [34] Zhang X, Tu J, He T, et al. Cascading texture evolution driven by dynamic competition of deformation mechanisms in Inconel 625 Ni-based superalloy prepared by laser powder bed fusion. *Mater Charact.* **2025**;229:115582.
- [35] Zhou L, Peng Z, Chen J, et al. The evolution of microstructure and mechanical properties of Inconel 625 alloy fabricated by laser powder bed fusion via novel hybrid scanning strategy. *Mater Sci Eng A.* **2024**;911:146925.
- [36] Liu X, Fan J, Song Y, et al. High-temperature tensile and creep behaviour of Inconel 625 superalloy sheet and its associated deformation-failure micromechanisms. *Mater Sci Eng A.* **2022**;829:142152.
- [37] Dai Z, Su Y, Yang T, et al. Study on the high temperature creep deformation and fracture behaviors of Inconel 625 deposited metal. *Mater Sci Eng A.* **2022**;854:143626.
- [38] Liu X, Fan J, Cao K, et al. Creep anisotropy behavior, deformation mechanism, and its efficient suppression method in Inconel 625 superalloy. *J Mater Sci Technol.* **2023**;133:58–76.
- [39] Xiao-An Hu G-LZ, Jiang Y, Ma X-F, et al. Experimental investigation on the LCF behavior affected by manufacturing defects and creep damage of one selective laser melting nickel-based superalloy at 815°C. *Acta Metall Sin.* **2020**;33(4):514–527.
- [40] Lass EA, Stoudt MR, Williams ME, et al. Formation of the Ni<sub>3</sub>Nb δ-phase in stress-relieved Inconel 625 Produced via Laser powder-bed fusion additive manufacturing. *Metal Mater Trans A.* **2017**;48(11):5547–5558.
- [41] Ruiz A, Rodríguez VM, Becerra HG, et al. Ultrasonic characterization of microstructural changes due to static recrystallization and grain growth in Inconel 625 and Inconel 718 superalloys. *Ultra.* **2024**;142:107383.
- [42] Hu YL, Li YL, Zhang SY, et al. Effect of solution temperature on static recrystallization and ductility of Inconel 625 superalloy fabricated by directed energy deposition. *Mater Sci Eng A.* **2020**;772:138711.
- [43] Sui S, Chen J, Li Z, et al. Investigation of dissolution behavior of laves phase in Inconel 718 fabricated by laser directed energy deposition. *Add Manuf.* **2020**;32:101055.
- [44] Li Z, Lin X, Yang H, et al. Anisotropic tensile properties and in-situ deformation behavior of Inconel 718 alloy fabricated by laser directed energy deposition. *J Alloys Compd.* **2024**;1007:176350.
- [45] Wang B, Huang R, Sun Y, et al. Hot isostatic pressing temperature effects on the microstructure and mechanical properties of laser powder bed fusion-manufactured Hastelloy X. *Eng Sci Addit Manuf.* **2025**;1:2.
- [46] Pathak P, Majkic G, Selvamannickam V. Role of customized scan strategies and dwell time on microstructure and properties of additively manufactured 316L stainless steel. *Mater Sci Addit Manuf.* **2024**;3:1.
- [47] Lin H, Dai C, Zhai W, et al. Additively manufactured Inconel 718 plus superalloy with heterostructures and high mechanical properties. *Mater Sci Eng A.* **2025**;924:147683.
- [48] Buffat PA, Alexandrou I, Czyska-Filemonowicz A. Composition and element distribution mapping of γ'

- and  $\gamma'$  phases of Inconel 718 by high-resolution scanning transmission electron microscopy and X-ray energy-dispersive spectrometry. *Materials*. 2024;17(3):594.
- [49] Dai S, Zhu J, Wu S, et al. Strength-ductility synergy in an additively manufactured oxide dispersion strengthened Inconel 718 superalloy at 650°C. *Mater Sci Eng A*. 2025;946:149135.
- [50] Li Z, Chen J, Sui S, et al. The microstructure evolution and tensile properties of Inconel 718 fabricated by high-deposition-rate laser directed energy deposition. *Add Manuf*. 2020;31:100941.
- [51] Sui S, Li Z, Zhong C, et al. Laves phase tuning for enhancing high temperature mechanical property improvement in laser directed energy deposited Inconel 718. *Compos B Eng*. 2021;215:108819.
- [52] Liu F, Lyu F, Liu F, et al. Laves phase control of inconel 718 superalloy fabricated by laser direct energy deposition via  $\delta$  aging and solution treatment. *J Mater Res Technol*. 2020;9(5):9753–9765.
- [53] Mataveli Suave L, Cormier J, Bertheau D, et al. High temperature low cycle fatigue properties of alloy 625. *Mater Sci Eng A*. 2016;650:161–170.
- [54] Mignanelli PM, Jones NG, Pickering EJ, et al. Gamma-gamma prime-gamma double prime dual-superlattice superalloys. *Scr Mater*. 2017;136:136–140.
- [55] Sundararaman M, Mukhopadhyay P, Banerjee S. Precipitation of the  $\delta$ -Ni<sub>3</sub>Nb phase in two nickel base superalloys. *Metall Trans A*. 1988;19(3):453–465.
- [56] Zhang Y, Lan L, Shi Q, et al. Optimization of mechanical properties of laser direct energy deposition repaired Inconel 718 alloy based on adjustment of Laves phase and  $\delta$  phase. *Mater Sci Eng A*. 2025;948:149310.
- [57] Kuo CM, Yang YT, Bor HY, et al. Aging effects on the microstructure and creep behavior of Inconel 718 superalloy. *Mater Sci Eng A*. 2009;510-511:289–294.
- [58] Chang L, Sun W, Cui Y, et al. Effect of heat treatment on microstructure and mechanical properties of the hot-isostatic-pressed Inconel 718 powder compact. *J Alloys Compd*. 2014;590:227–232.
- [59] Sui S, Chen J, Ma L, et al. Microstructures and stress rupture properties of pulse laser repaired Inconel 718 superalloy after different heat treatments. *J Alloys Compd*. 2019;770:125–135.
- [60] He LZ, Zheng Q, Sun XF, et al. Effect of carbides on the creep properties of a Ni-base superalloy M963. *Mater Sci Eng A*. 2005;397(1):297–304.
- [61] Zhang L, Hu Z, Zhang L, et al. Enhancing the strength-ductility trade-off in a NiCoCr-based medium-entropy alloy with the synergetic effect of ultra fine precipitates, stacking faults, dislocation locks and twins. *Scr Mater*. 2022;211:114497.
- [62] Grässel O, Krüger L, Frommeyer G, et al. High strength Fe–Mn–(Al, Si) TRIP/TWIP steels development – properties – application. *Int J Plast*. 2000;16(10):1391–1409.
- [63] Bouaziz O, Guelton N. Modelling of TWIP effect on work-hardening. *Mater Sci Eng A*. 2001;319-321:246–249.
- [64] Hu YL, Lin X, Lu XF, et al. Evolution of solidification microstructure and dynamic recrystallisation of Inconel 625 during laser solid forming process. *J Mater Sci*. 2018;53(22):15650–15666.
- [65] Wu G, Tang J, Wang N, et al. Effect of strain rate-induced microstructure on mechanical behavior of dual-phase steel. *J Mater Res Technol*. 2022;18:2093–2103.
- [66] Li Y, Jiang Z, Li L, et al. Dynamic recovery and recrystallization of an as-cast SX superalloy during hot deformation. *J Mater Sci Technol*. 2025;217:296–310.
- [67] Zhang H, Chen K, Pantleon W, et al. High-temperature deformation of Ni-based superalloy and recrystallization prevention by recovery. *Scr Mater*. 2025;265:116732.